



Enhanced moisture resistance and catalytic stability of ethylene oxidation at room temperature by the ultrasmall MnO_x cluster/Pt hetero-junction

Zhiquan Hou¹, Meiqi Chen¹, Yuxi Liu^{*}, Jiguang Deng, Lin Jing, Ruyi Gao, Wenbo Pei, Zeya Li, Hongxing Dai^{*}

Key Laboratory of Beijing on Regional Air Pollution Control, Beijing Key Laboratory for Green Catalysis and Separation, Key Laboratory of Advanced Functional Materials, Education Ministry of China, Department of Chemical Engineering, Faculty of Environment and Life, Beijing University of Technology, Beijing 100124, China



ARTICLE INFO

Keywords:

Bimetallic nanoparticle
Supported noble metal catalyst
Ethylene oxidation
Isotopic trace
Water resistance

ABSTRACT

Ethylene elimination can effectively inhibit the rapid aging of fruits and vegetables in storage and transportation. Improving the low-temperature activity, moisture resistance, and stability of Pt based catalysts is a challenge for catalytic oxidation of ethylene which is an effective elimination method. Herein, we constructed ultrasmall MnO_x cluster ($< 1 \text{ nm}$) on Pt particles via an alloy *in situ* transformation strategy, which created a large number of MnO_x/Pt interfaces. Among all of the samples, $1.89\text{Pt}_{2.20}\text{Mn}/\text{TiO}_2$ showed the highest catalytic activity in the oxidation of ethylene at a space velocity of $20,000 \text{ mL}/(\text{g h})$: $T_{50\%} = 34^\circ\text{C}$ and $T_{90\%} = 43^\circ\text{C}$, specific reaction rate at $35^\circ\text{C} = 33.0 \mu\text{mol}/(\text{g}_\text{Pt} \text{ s})$, and turnover frequency at $35^\circ\text{C} = 6.5 \times 10^{-3} \text{ s}^{-1}$. In addition, $\text{Pt}_{2.20}\text{Mn}/\text{TiO}_2$ also exhibited better water resistance and stability than Pt/TiO_2 . The results of XPS, $\text{H}_2\text{O-TPD}$, $\text{C}_2\text{H}_4\text{-TPD}$, *in situ* DRIFTS, and H_2^{18}O isotopic tracing characterization revealed that the MnO_x/Pt interfacial sites accelerated desorption of CO_2 and enhanced the activation of surface active oxygen species (O_2 to O_2^{2-}). Meanwhile, the numerous interfaces provide more active sites for ethylene adsorption and activation, reducing the inhibitory effect of adsorbed water on ethylene adsorption. It was concluded that the prohibited CO_2 adsorption, and increased adsorbed oxygen species were responsible for the excellent catalytic performance and good stability of $1.89\text{Pt}_{2.20}\text{Mn}/\text{TiO}_2$, while the more active sites for ethylene adsorption and activation were responsible for the good water resistance of $1.89\text{Pt}_{2.20}\text{Mn}/\text{TiO}_2$.

1. Introduction

Ethylene is one of volatile organic compounds that can accelerate aging and decaying of fruits and vegetables (F&V). Hence, it is highly desired to eliminate low-concentration ethylene for the storage and transportation of F&V. Among the ethylene removal methods, catalytic oxidation is one of the most effective pathways, in which the critical issue is the availability of high-performance catalysts. For example, Ahn et al. [1] adopted the deposition method to prepare the $\text{Au}/\text{Co}_3\text{O}_4$ catalysts, and found that ethylene could be totally oxidized at 165°C . By loading cobalt oxide on mesoporous carbon spheres, Li et al. [2] claimed that ethylene was completely oxidized at 185°C . Isaifan et al. [3] reported that catalytic activity of Pt/C was related to the size of Pt particles, with the Pt/C sample with the smallest Pt size ($1.5 \pm 0.5 \text{ nm}$) exhibiting the best catalytic performance for ethylene oxidation (ethylene complete conversion temperature was 90°C). Qiao and

coworkers [4,5] loaded Au nanoparticles (NPs) on Fe_2O_3 , Co_3O_4 , TiO_2 , and ZnO , and observed that the complete oxidation of ethylene could be achieved at 300°C over 2 wt% Au/ZnO , 250°C over 2 wt% Au/TiO_2 , 210°C over 2 wt% $\text{Au}/\text{Fe}_2\text{O}_3$, and 160°C over 2 wt% $\text{Au}/\text{Co}_3\text{O}_4$.

Usually, the storage and transportation of F&V are carried out at low temperatures, in which there is the presence of water vapor. Hence, the low-temperature activity, water resistance, and catalytic stability of the catalyst are important in its practical applications. Ma and coworkers [6] have made intensive investigations on stability and water resistance of the supported catalysts for ethylene combustion. For example, they observed that ethylene could be totally oxidized over $\text{Au}/\text{meso-Co}_3\text{O}_4$ at 0°C , which was due to the active exposed (110) crystal plane of meso- Co_3O_4 and highly dispersed Au NPs, but stability of this catalyst was poor. The commonly used strategy for regulating stability and water resistance is to regulate the acid sites of the catalyst to achieve the regulation of water adsorption and desorption ability. Such as, Ma and

* Corresponding authors.

E-mail addresses: yxliu@bjut.edu.cn (Y. Liu), hxdai@bjut.edu.cn (H. Dai).

¹ These authors contributed equally to this work.

coworkers reported the Ag/ZSM-5 [7,8] and Pt/F-ZSM-5 [9] catalysts, and found that such porous materials could effectively catalyze the oxidation of ethylene (the complete conversion temperature was 25 °C), with the Ag/ZSM-5 (SiO₂/Al₂O₃ ratio = 38) and 0.5 wt% Pt/F-ZSM-5 catalysts possessing the best stability since there were slow adsorption and rapid desorption of water on/from the Ag/ZSM-5 sample [7,8] and the doping of F increased amount of the Brønsted acid sites (which favored the adsorption and activation of ethylene) hence extending the lifetime and improving water resistance of 0.5 wt% Pt/F-ZSM-5 [9].

Usually, supported single noble metal NPs tend to grow into large particles, leading to their deactivation. However, the doping of the second metal to a noble metal can reduce the cost of a supported noble metal catalyst and enhance its catalytic activity, stability, and water resistance due to the presence of synergistic action between the two metals. For instance, Kang et al. [10] reported that Pt₃Zn/C outperformed PtZn/C and the supported PtZn bimetallic catalysts exhibited better anti-poisoning performance than Pt/C in methanol oxidation. Working on CO oxidation over the Fe/CeO₂, and Cu/CeO₂, and Fe-Cu/CeO₂ catalysts, Hinokuma et al. [11] pointed out that Fe-Cu/CeO₂ outperformed Fe/CeO₂ and Cu/CeO₂. After investigating the Fe-Co/SiO₂, Co-Ni/SiO₂, Ni-Fe/SiO₂, and SiO₂-supported Fe, Co, Ni, and Cu catalysts, Ishihara et al. [12] found that the supported bimetallic catalysts showed better activities than the supported single metal catalysts for the Fischer-Tropsch synthesis. Sun et al. [13] claimed that PdCo/C was superior to Pd/C in catalyzing the oxidation of HCOOH. By loading Pt₃Co NPs on the surface of SiO₂, Al₂O₃, MgO, CaO or Al₂O₃, Furukawa et al. [14] observed that the supported Pt₃Co bimetallic catalysts showed better activities than the supported Pt catalyst for CO oxidation, with Pt₃Co/MgO performing the best. By adopting the co-precipitation method to generate the RuMo/Al₂O₃ catalysts, Adamska et al. [15] pointed out that RuMo/Al₂O₃ with an appropriate doping of Mo was more active and more catalytically stable than Ru/Al₂O₃ in the oxidation of propane.

The oil-phase reduction method is an effective strategy in synthesizing monodispersive metal particles. For example, Zhu et al. [16] first adopted the oil-phase method to synthesize the PtFe nanowires, and then loaded them on the surface of TiO₂. These authors found that CO could be totally oxidized over PtFe/TiO₂ at room temperature, and activity and stability of this sample were much better than those of the supported Pt sample. Working on the loading of Ag, Au, AgAu NPs on Al₂O₃, TiO₂ or CeO₂, Rojuechai et al. [17] claimed that AgAu/Al₂O₃ performed the best for the epoxidation of ethylene, which was associated with the particle size of the well-dispersed AgAu NPs and the interaction between AgAu NPs and Al₂O₃.

In the past several years, our group has investigated some supported bimetallic catalysts for the oxidation of organics. For instance, Yang et al. [18] prepared the Pt_xCo/meso-MnO_y catalysts, and observed that 0.70 wt% Pt_{2.42}Co/meso-MnO_y outperformed 0.66Pt/meso-MnO_y for methanol oxidation. After studying the oxidation of toluene over the Au-Pd/3DOM Co₃O₄ catalysts, Xie et al. [19] pointed out that Au-Pd/3DOM Co₃O₄ showed better activities than Au/3DOM Co₃O₄ and Pd/3DOM Co₃O₄. Working on methane combustion over Pd-GaO_x/Al₂O₃, Hou et al. [20] reported that the better activity of Pd-GaO_x/Al₂O₃ than that of Pd/Al₂O₃ was due to the more amount of oxygen vacancies and the formation of the surface Pd-O-Ga-like bond in/on the former catalyst. Liang et al. [21] used the oil-phase and impregnation methods to synthesize TiO₂-supported PdW bimetallic ultrathin nanosheets (in which the W was highly distributed), and found that PdW/TiO₂ was superior to Pd/TiO₂ in catalytic activity and water resistance, which was related to its redox cycle of surface Pd²⁺/Pd⁰, low-temperature reducibility, and synergistic action between Pd(O) or WO_x and TiO₂. Furthermore, the good water resistance was due to the timely replenishing of lattice oxygen in PdO_x consumed during the benzene oxidation process. In one of our works on PtMo/Al₂O₃ for benzene oxidation [22], we concluded that the better activity of PtMo/Al₂O₃ than that of Pt/Al₂O₃ was associated with the active oxygen

species (O⁻, O₂⁻ or O₂²⁻) formed at the Pt site in PtMo/Al₂O₃ and the effective transfer and activation of benzene and O₂ at the Pt-MO_x interfaces.

In the present work, we first adopted the oil-phase reduction method to fabricate the Pt_xMn nanocrystals, and then used the impregnation method to prepare the titania-supported Pt_xMn catalysts, characterized their physicochemical properties, evaluated their catalytic activities for ethylene oxidation, and examined water resistance of the as-prepared typical catalyst. It was found that 1.89Pt_{2.20}Mn/TiO₂ possessed better activity, stability, and water resistance than 1.91Pt/TiO₂.

2. Experimental

2.1. Catalyst preparation

2.1.1. Synthesis of Pt and Pt_xMn NPs

0.10 mol of platinum 2,4-pentanedionate was first added to the mixture of 5 mL of diphenyl ether, 3.68 mL of oleylamine, and 0.63 mL of oleic acid, and stirred for 5 min. The temperature of the mixed solution was increased to 265 °C under the protection of nitrogen, and the mixed solution was further stirred for 10 min, which was denoted as solution A. 0.20 g of borane-tert-butylamine complex or 0.025 mmol of manganese carbonyl was added to 6.0 mL of oleylamine so that it was completely dissolved under stirring, thus obtaining solution B. Then, solution B was added to solution A which was maintained in N₂ at 265 °C for 10 min, and kept at 265 °C for 1 h of reaction, followed by cooling down to room temperature (RT). The obtained mixed solution was centrifuged and washed with cyclohexane two times, thus obtaining the uniformly sized Pt and Pt₂Mn (theoretical Pt/Mn molar ratio = 2/1) NPs, respectively. Similarly, we synthesized the uniformly sized PtMn (theoretical Pt/Mn molar ratio = 1/1) and Pt₂Mn₃ (theoretical Pt/Mn molar ratio = 2/3) NPs by adopting the above same procedures with molar ratios of platinum 2,4-pentanedionate to manganese carbonyl different from 0.10: 0.025–0.10: 0.05 and 0.10: 0.15, respectively. Finally, the obtained Pt and Pt_xMn NPs were dispersed in cyclohexane, respectively.

2.1.2. Preparation of TiO₂-supported Pt and Pt_xMn NPs

1.00 g of TiO₂ was first added to the Pt-, Pt₂Mn-, PtMn-, and Pt₂Mn₃ NPs-containing cyclohexane and stirred for 8 h. After being filtered, the obtained solid was put in an oven for calcination at a ramp of 5 °C/min from RT to 300 °C and maintained at 300 °C for 6 h, hence obtaining the Pt/TiO₂, Pt₂Mn/TiO₂, PtMn/TiO₂, and Pt₂Mn₃/TiO₂, respectively. The inductively coupled plasma-atomic emission spectroscopic (ICP-AES) results reveal that the actual chemical compositions of the as-obtained samples were 1.91 wt% Pt/TiO₂, 1.89 wt% Pt_{2.20}Mn/TiO₂, 1.92 wt% Pt_{1.10}Mn/TiO₂, and 1.92 wt% Pt_{0.67}Mn/TiO₂, which were denoted as 1.91Pt/TiO₂, 1.89Pt_{2.20}Mn/TiO₂, 1.92Pt_{1.10}Mn/TiO₂, and 1.92Pt_{0.67}Mn/TiO₂, respectively. It should be noted that the number before the sample name means the loading of Pt in Pt/TiO₂ or the total loading of Pt and Mn in Pt_xMn/TiO₂.

2.1.3. Preparation of TiO₂-supported MnO_x

5 mL of diphenyl ether, 3.68 mL of oleylamine, and 0.63 mL of oleic acid were first well mixed under stirring for 5 min. The temperature of the mixed solution was increased to 265 °C under the protection of nitrogen, and the mixed solution was further stirred for 10 min, which was denoted as solution A. 1.00 g of manganese carbonyl was added to 6.0 mL of oleylamine so that it was completely dissolved under stirring, thus obtaining solution B. Then, solution B was added dropwise to solution A which was maintained in N₂ at 265 °C for 10 min, and kept at 265 °C for 1 h of reaction, followed by cooling down to RT. The obtained mixed solution was centrifuged and washed with cyclohexane two times, thus obtaining the uniformly sized Mn NPs. Finally, the obtained Mn NPs were dispersed in cyclohexane. 1.00 g of TiO₂ was first added to the Mn NPs-containing cyclohexane and stirred for 8 h. After being filtered, the

obtained solid was put in an oven for calcination at a ramp of 5 °C/min from RT to 300 °C and maintained at 300 °C for 6 h, hence obtaining the MnO_x/TiO₂ sample. The ICP–AES measurement reveals that the actual chemical composition of this sample was 2.00 wt% MnO_x/TiO₂ (denoted as 2.00MnO_x/TiO₂).

2.2. Catalyst characterization

Physicochemical properties of the samples were characterized by means of the techniques, such as the ICP–AES, X-ray diffraction (XRD), Raman spectra, transmission electron microscopy (TEM), high-angle annular dark field–scanning transmission electron microscopic (HAADF–STEM), energy dispersive X-ray spectroscopy (EDX) element mapping, N₂ adsorption–desorption (BET), X-ray photoelectron spectroscopy (XPS), X-ray absorption fine structure (XAFS), thermogravimetric analysis (TGA), Fourier transform infrared spectroscopy of pyridine adsorption (Pyridine-FTIR), temperature-programmed desorption of water, ethylene or ethylene and water (H₂O, C₂H₄- or C₂H₄–H₂O-TPD), temperature-programmed surface reaction of ethylene and H¹⁸O ((C₂H₄ + H¹⁸O)-TPSR), and in situ diffuse reflection Fourier transform infrared spectroscopy (in situ DRIFTS). The detailed characterization procedures are described in the [Supplementary material](#).

2.3. Catalytic activity measurement

Catalytic activities of the samples for ethylene oxidation were measured in a continuous flow fixed-bed quartz microreactor (i.d. = 6 mm) at atmospheric pressure. 50 mg of the sample (40–60 mesh) well mixed with 250 mg of quartz sand (40–60 mesh) was loaded in the microreactor, the reactant gas mixture was composed of 500 ppm C₂H₄ + 20 vol% O₂ + He (balance), and the space velocity was 20,000 mL/(g h). Prior to the activity measurement, the temperature of the catalyst bed was increased in an (20 vol% O₂ + He (balance)) flow of 20 mL/min at a ramp of 5 °C/min from RT to 200 °C and the catalyst bed was kept at 200 °C for 1 h. Effects of water vapor and carbon dioxide on catalytic activity of the typical sample were also examined, in which 50 RH% water vapor or 3 vol% CO₂ was introduced to the reaction system. The concentrations of reactants and products were analyzed by gas chromatography (GC-2014 C, Shimadzu) with a flame ionization detector (FID), using a stabilwax-DA column (30 m in length) and a Carboxen 1000 column (3 m in length). The balance of carbon throughout the catalytic system was estimated to be 98.5 ± 1.5%. The temperatures (T_{10%}, T_{50%}, and T_{90%}) required for achieving ethylene conversions of

10%, 50%, and 90%, specific reaction rate, and turnover frequency (TOF_{Pt}) were used to evaluate catalytic activities of the samples, respectively. TOF_{Pt} = $xC_0/(n_{Pt} D_{Pt})$, where x , C_0 (mol/s), n_{Pt} (mol), and D_{Pt} represent the conversion at 35 °C, initial ethylene concentration, actual Pt molar amount, and metal dispersion, respectively.

3. Results and discussion

3.1. Crystal phase composition and morphology

Fig. 1 shows XRD patterns of the as-synthesized metal NPs and TiO₂-supported metal samples. It is seen from **Fig. 1A** that Pt, Pt_{2.20}Mn, Pt_{1.10}Mn, and Pt_{0.67}Mn NPs display the diffraction peaks at $2\theta = 39.7^\circ$, 46.2° , and 67.4° (corresponding to the (111), (200), and (220) crystal planes), which are characteristic signals of a cubic Pt phase. With the rise in Mn content of Pt_xMn NPs, intensity of the peaks at $2\theta = 34.9^\circ$, 40.5° , 58.7° , and 70.2° (corresponding to the (111), (200), (220), and (311) crystal planes) that were assigned to the cubic MnO phase increased. It can be also observed from **Fig. 1B** that there are XRD signals at $2\theta = 25.3^\circ$, 37.8° , 48.0° , 53.9° , 55.1° , 62.7° , 68.8° , 70.3° , and 75.0° , attributable to the anatase TiO₂ in the 1.91Pt/TiO₂, 1.89Pt_{2.20}Mn/TiO₂, 1.92Pt_{1.10}Mn/TiO₂, and 1.92Pt_{0.67}Mn/TiO₂ samples; furthermore, two peaks at $2\theta = 39.7^\circ$ and 46.2° are recorded, which are due to the (111) and (200) crystal planes of the cubic Pt phase.

Shown in **Fig. 2** are TEM images and elemental mappings of the metal NPs. Obviously, all of the monodispersed Pt, Pt_{2.20}Mn, Pt_{1.10}Mn, and Pt_{0.67}Mn NPs displayed a cube-like morphology and were uniform in particle size. After statistical analysis on the metal NPs in TEM images, we can realize that the average sizes of Pt, Pt_{2.20}Mn, Pt_{1.10}Mn, and Pt_{0.67}Mn NPs are 7.8, 6.5, 5.9, and 7.6 nm (**Fig. S1**), respectively.

Fig. 2E–H and **Fig. S2** shows HAADF–STEM images, EDX elemental mappings, and EDX line scan of Pt_{2.20}Mn NPs. Apparently, Pt_{2.20}Mn NPs were composed of uniformly monodispersed cube-like particles (**Fig. 2E**). There were Pt and Mn elements in Pt_{2.20}Mn NPs (**Fig. 2D, F**). Furthermore, the EDX line scan of Pt_{2.20}Mn NPs (**Fig. 2F**) indicates that Pt and Mn are distributed in a core-shell-like structure.

3.2. Oxidation state and microstructure of platinum in 1.89Pt_{2.20}Mn/TiO₂ and 1.91Pt/TiO₂

Fig. 3A–D and **Fig. S3** shows microstructures of the 1.89Pt_{2.20}Mn/TiO₂ sample determined using the aberration-corrected HAADF–STEM (ac-HAADF–STEM) and EDX techniques. After loading of the metal NPs

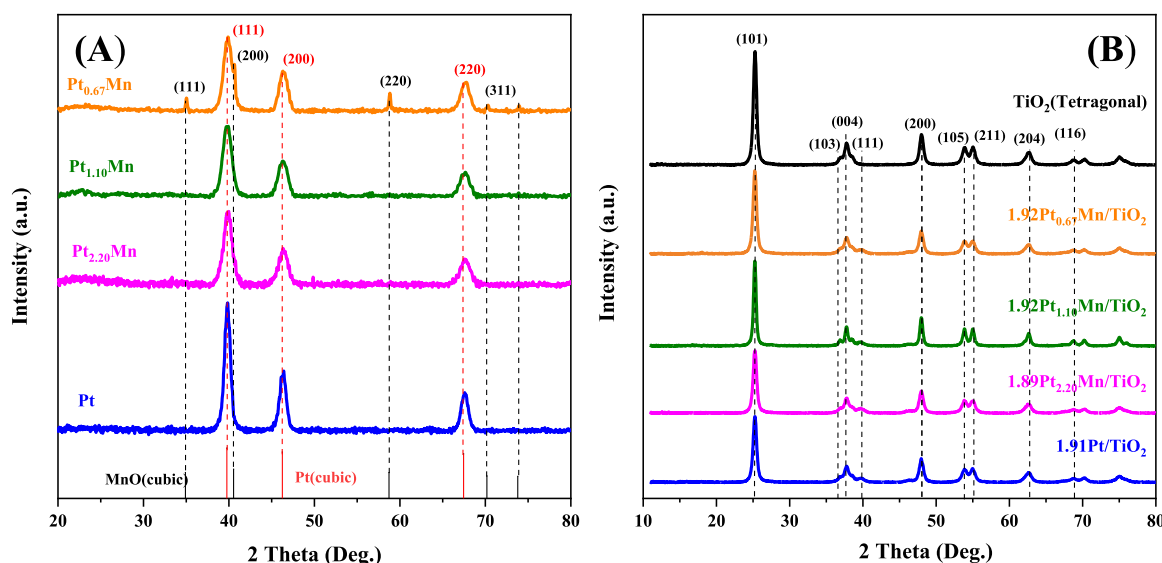


Fig. 1. XRD patterns of (A) the as-synthesized metal NPs and (B) TiO₂-supported metal nanocatalysts.

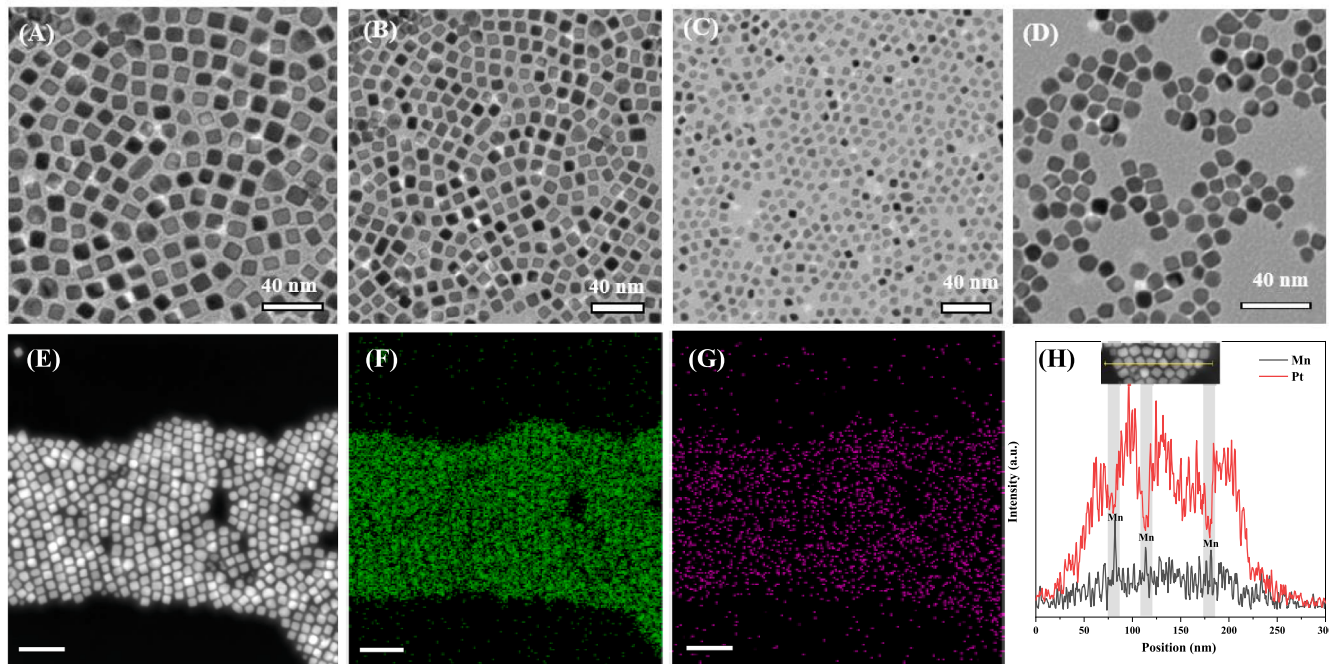


Fig. 2. TEM images of (A) Pt NPs, (B) $\text{Pt}_{2.20}\text{Mn}$ NPs, (C) $\text{Pt}_{1.10}\text{Mn}$ NPs, and (D) $\text{Pt}_{0.67}\text{Mn}$ NPs, and (E) HAADF-STEM images, (F, G) EDX elemental mappings, and (H) EDX line scan of $\text{Pt}_{2.20}\text{Mn}$ NPs.

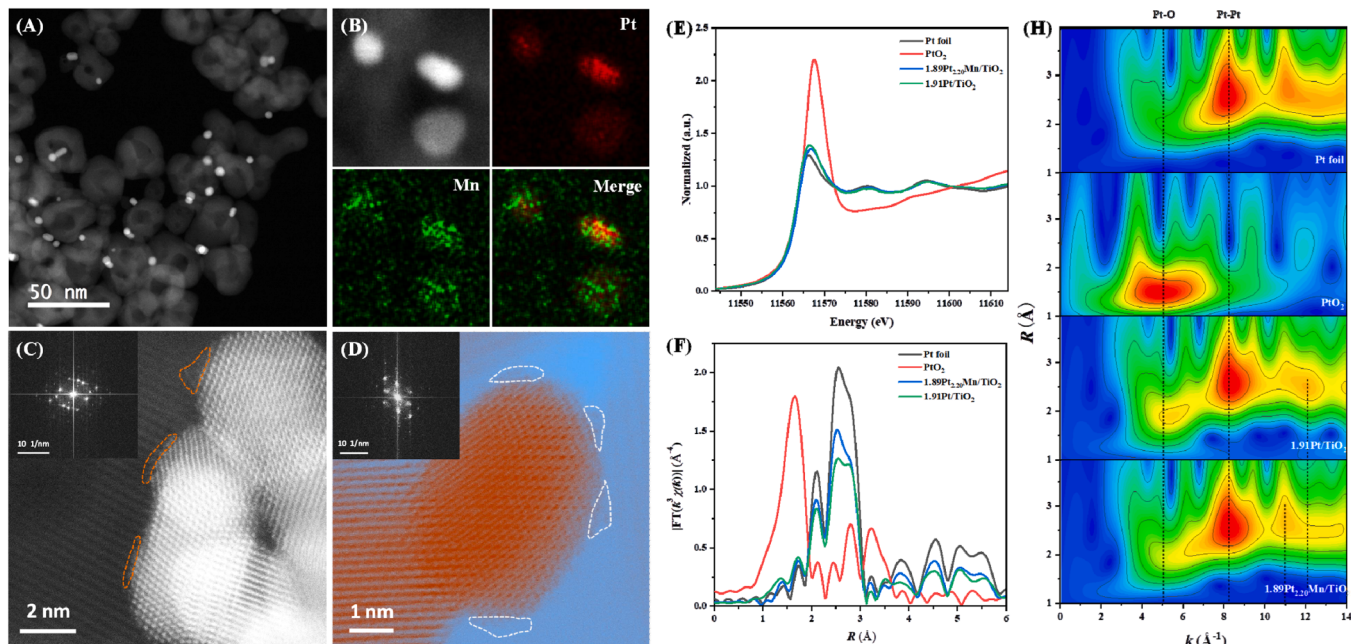


Fig. 3. —(A) HAADF-STEM images, (B) EDX elemental mappings, and (C, D) ac-HAADF-STEM images and selected-area electron diffraction (insets) of $1.89\text{Pt}_{2.20}\text{Mn}/\text{TiO}_2$, (E) XANES spectra, (F) Fourier transform (FT) k^2 -weighted $\chi(k)$ -function of the EXAFS spectra, and (H) wavelet transforms for the Pt L_{III} -edge of $1.89\text{Pt}_{2.20}\text{Mn}/\text{TiO}_2$ and $1.91\text{Pt}/\text{TiO}_2$.

on the surface of TiO_2 , morphologies of the samples are shown in Fig. S3. The morphology of $\text{Pt}_{2.20}\text{Mn}$ NPs in $1.89\text{Pt}_{2.20}\text{Mn}/\text{TiO}_2$ was cubic, and their average particle size was approximately 6.5 nm. As shown in the EDX mappings (Fig. 3B), the Mn was dispersed on the surface of Pt particles, ~ 1 nm in size. The ac-HAADF-STEM (Fig. 3C and D) images show the microstructures of bimetal nanoparticles. Due to the atomic number of Mn is much smaller than that of Pt, Mn atoms show a lower contrast than Pt atoms. It can be observed that some darker clusters (circled by yellow or white lines) are seen on the Pt nanoparticles, whose

average size is close to 1 nm. Besides, these clusters were also confirmed by the EDX mappings (Fig. 3B and S4). The Mn in the form of clusters or small particles was dispersed on the surface of Pt particles. After measurement, the average particle size of clusters or small particles was approximately 1 nm. These results indicate there are ultra-thin MnO_x layers on Pt particles. The XAFS technique was used to study the fine structure of the typical samples and the interaction between Pt and Mn. Fig. 3E shows XANES spectra of the $1.89\text{Pt}_{2.20}\text{Mn}/\text{TiO}_2$ and $1.91\text{Pt}/\text{TiO}_2$ samples as well as the referenced Pt foil and PtO_2 samples. As well

known, a key feature of these spectra is the white line, which is an important indication of the Pt oxidation state [23]. From the XANES spectra of the 1.89Pt_{2.20}Mn/TiO₂ and 1.91Pt/TiO₂ samples (Fig. 3E), we can see that intensity of the white line is close to that in Pt foil, demonstrating that most of the Pt in 1.89Pt_{2.20}Mn/TiO₂ and 1.91Pt/TiO₂ are Pt⁰. However, the Pt became slightly less oxidized as indicated by the decrease in the white line intensity of 1.89Pt_{2.20}Mn/TiO₂, compared with that of 1.91Pt/TiO₂. Fig. 3F, S5, and H shows Fourier transform (FT) k^2 -weighted $\chi(k)$ -function of the EXAFS spectra and wavelet transforms for Pt L_{III} -edge of the Pt foil, PtO₂, 1.89Pt_{2.20}Mn/TiO₂, and 1.91Pt/TiO₂ samples, and Table S1 summarizes their EXAFS curve-fitting results. The coordination numbers of the Pt–Pt bond in Pt foil, 1.89Pt_{2.20}Mn/TiO₂, and 1.91Pt/TiO₂ were approximately 12.0, 10.6, and 9.4, whereas those of the Pt–O bond in PtO₂, 1.89Pt_{2.20}Mn/TiO₂, and 1.91Pt/TiO₂ were 5.0, 0.3, and 0.6, respectively. The oxidation of the Pt particles leads to a decrease in Pt–Pt coordination number of 1.91Pt/TiO₂ [24]. As shown in Fig. 3H, however, the surface Pt atoms coordinate with Mn atoms due to the presence of Mn clusters on the surface of Pt particles in 1.89Pt_{2.20}Mn/TiO₂. The fraction of coordinately unsaturated surface Pt atoms on 1.89Pt_{2.20}Mn/TiO₂ decreased, which was different with that on 1.91Pt/TiO₂. Hence, the larger coordination number of the Pt–Pt bonds and fewer number of the Pt–O bonds were formed on the surface of 1.89Pt_{2.20}Mn/TiO₂.

3.3. Catalytic performance

The oxidation of ethylene was selected as a model reaction to evaluate catalytic performance of the samples. Fig. 4A shows catalytic

activities of the as-fabricated samples for ethylene oxidation at a SV of 20,000 mL/(g h). It is obvious that ethylene conversion over each sample increases with the rise in temperature. We use the temperatures ($T_{50\%}$ and $T_{90\%}$) required for achieving ethylene conversions of 50% and 90% to evaluate catalytic activity of a sample, respectively, and catalytic activities of all of the samples are summarized in Table 1. The $T_{50\%}$ and $T_{90\%}$ were 34 and 43 °C over 1.89Pt_{2.20}Mn/TiO₂, 45 and 55 °C over 1.92Pt_{1.10}Mn/TiO₂, 41 and 49 °C over 1.92Pt_{0.67}Mn/TiO₂, 53 and 58 °C over 1.91Pt/TiO₂, and 115 and 135 °C over 2.00MnO_x/TiO₂, respectively. Meanwhile, the TOF or specific reaction rate of the catalyst showed a significant increase with the introduction of Mn, compared with 1.91Pt/TiO₂. 1.89Pt_{2.20}Mn/TiO₂ exhibited the highest specific reaction rate (33.0×10^{-6} mol/(g_{Pt} s) and TOF_{Pt} (6.5×10^{-3} s⁻¹) at 35 °C, which were much higher than those (1.4×10^{-6} mol/(g_{Pt} s) and 0.3×10^{-3} s⁻¹, respectively) of 1.91Pt/TiO₂. In other words, catalytic activity decreased in the order of 1.89Pt_{2.20}Mn/TiO₂ > 0.92Pt_{0.67}Mn/TiO₂ > 1.92Pt_{1.10}Mn/TiO₂ > 1.91Pt/TiO₂. Therefore, the doping of Mn enhanced catalytic activity of the supported Pt sample.

In order to examine catalytic stability, the 30-h on-stream ethylene oxidation over the 1.91Pt/TiO₂, 1.89Pt_{2.20}Mn/TiO₂, and 1.92Pt_{0.67}Mn/TiO₂ samples were carried out (Fig. 4B). It is found that no significant alterations in ethylene conversion are detected over 1.89Pt_{2.20}Mn/TiO₂ and 1.92Pt_{0.67}Mn/TiO₂, but a gradual activity decline occurs over 1.91Pt/TiO₂ (e.g., ethylene conversion decreases from 85% to 55% after 30 h of on-stream reaction). The results demonstrate that the doping of Mn to Pt can improve catalytic stability of the sample. It should be pointed out that the products of ethylene oxidation are CO₂ and H₂O, and no any intermediates are detected, as revealed by the GC–MS results (Fig. S6).

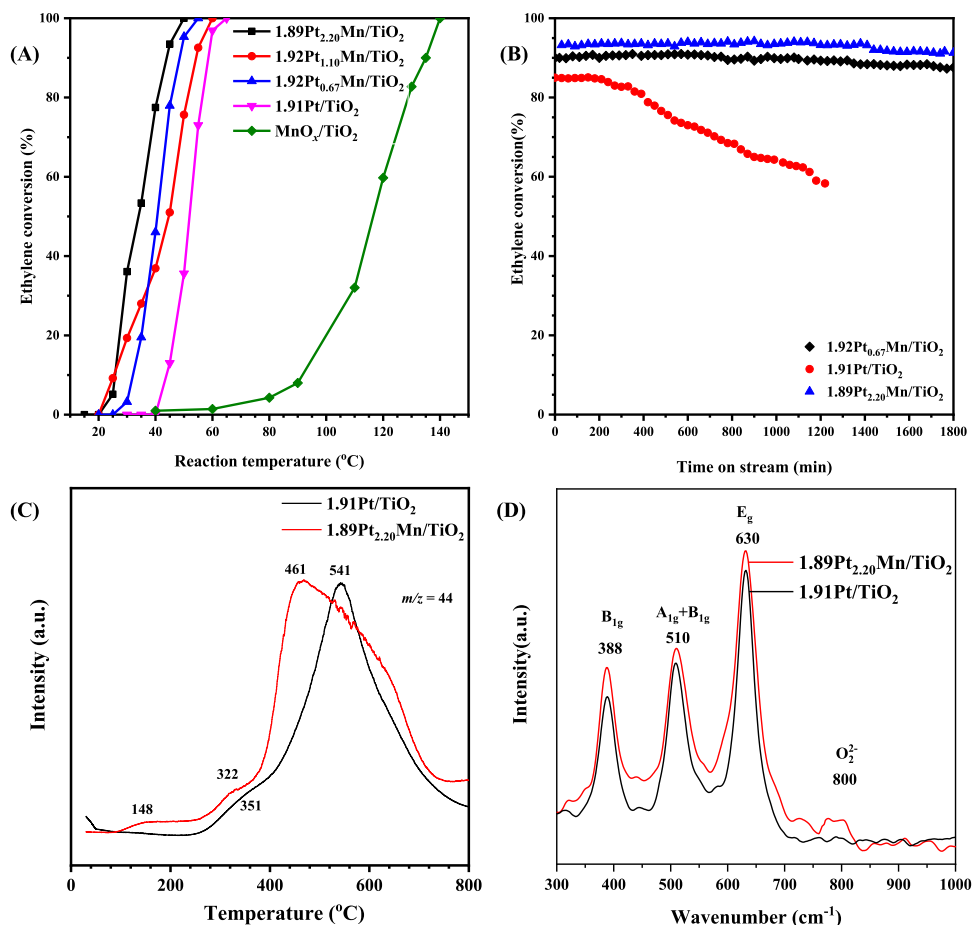


Fig. 4. Ethylene conversion as a function of (A) temperature or (B) on-stream reaction time over the samples at SV = 20,000 mL/(g h), and (C) CO₂ desorption profiles and (D) Raman spectra of C₂H₄-TPD over 1.89Pt_{2.20}Mn/TiO₂ and 1.91Pt/TiO₂.

Table 1

Average particle sizes, actual metal loadings, O_{ads}/O_{latt} molar ratios, catalytic activities, specific reaction rates and TOFs at 35 °C, and metal dispersion of the samples for ethylene oxidation at $SV = 20,000 \text{ mL}/(\text{g h})$.

Sample	Particle size ^a (nm)	Actual Pt loading ^b (wt %)	Actual Mn loading ^b (wt%)	Pt/Mn molar ratio ^b (mol/mol)	O_{ads}/O_{latt} molar ratio ^c (mol/mol)	Ethylene oxidation activity	Ethylene oxidation at 35 °C		Metal dispersion ^d (%)	
							$T_{50\%}$ (°C)	$T_{90\%}$ (°C)		
1.91Pt/TiO ₂	7.8	1.91	—	—	0.16	53	58	1.4	0.3	18
1.89Pt _{2.20} Mn/TiO ₂	6.5	1.68	0.21	2.20: 1.00	0.25	34	43	33.0	6.5	23
1.92Pt _{1.10} Mn/TiO ₂	5.9	1.53	0.39	1.10: 1.00	0.21	45	55	16.3	3.3	27
1.92Pt _{0.67} Mn/TiO ₂	7.6	1.35	0.57	0.67: 1.00	0.22	41	49	18.4	3.7	19
2.00MnO _x /TiO ₂	—	—	2.00	—	—	115	135	—	—	—

^a Data were measured according to the TEM images;

^b Data were determined by the ICP–AES technique;

^c Data were determined by the XPS technique;

^d Data were measured by the CO chemisorption.

In order to further understand the reason for the enhanced performance, the TPD and Raman experiments were conducted. As shown in Fig. 4C and S7, there were three CO₂ desorption peaks at 148, 322, and 461 °C, corresponding to the CO₂ signals generated via the reactions of the adsorbed oxygen, surface active lattice oxygen, and bulk lattice oxygen species with the adsorbed ethylene. The desorption peak of 1.89Pt_{2.20}Mn/TiO₂ or 1.92Pt_{0.67}Mn/TiO₂ appeared at a lower temperature than that of 1.91Pt/TiO₂; furthermore, intensity of the CO₂ desorption signal from the former two samples at low temperature (148 °C) was stronger than that from the latter sample. In addition, as shown in Fig. S8 and Table 1, a more amount (0.25) of the O_{ads} species on 1.89Pt_{2.20}Mn/TiO₂ was observed than that (0.16) on 1.91Pt/TiO₂. The O_{ads}/O_{latt} molar ratios on the other Mn-doped samples were similar to that on 1.89Pt_{2.20}Mn/TiO₂. The O_{ads}/O_{latt} molar ratio decreased in the sequence of 1.89Pt_{2.20}Mn/TiO₂ > 1.92Pt_{0.67}Mn/TiO₂ > 1.92Pt_{1.10}Mn/TiO₂ > 1.91Pt/TiO₂, similar to the changing trend in catalytic activity. In addition, O₂-TPD profiles of the different samples are shown in Fig. S9. The desorption temperatures of O₂ were 117, 273, 405, and 472 °C. As reported in the literature [20,25], the peaks at lower temperature (< 300 °C) were attributed to desorption of physically and chemically adsorbed oxygen species, whereas the peaks in the range of 300–700 °C were assigned to desorption of lattice oxygen species. It can be seen from Fig. S9 that the desorption temperatures of O₂ on the 1.89Pt_{2.20}Mn/TiO₂ and 1.91Pt/TiO₂ samples are similar. However, there was a more amount of oxygen desorbed from the 1.89Pt_{2.20}Mn/TiO₂ sample at low temperatures, indicating that there was a more amount of the oxygen species adsorbed on the 1.89Pt_{2.20}Mn/TiO₂ surface, which was in good agreement with the Raman and C₂H₄-TPD results.

In order to elucidate the oxygen species on the sample surface, the Raman spectra of the samples were recorded, as shown in Fig. 4D. The 1.89Pt_{2.20}Mn/TiO₂ and 1.91Pt/TiO₂ catalysts exhibited vibration bands at 388, 510, and 630 cm⁻¹, which were attributed to the B_{1g}, A_{1g} + B_{1g}, and E_g [26], respectively. The difference was that there was an additional vibration band (at 800 cm⁻¹) of the peroxide (O₂²⁻) species of 1.89Pt_{2.20}Mn/TiO₂ [27]. It means that the surface of 1.89Pt_{2.20}Mn/TiO₂ contains the O₂²⁻ species. Pu et al. [28] reported that the O₂²⁻ species could effectively promote the oxidation of ethylene. Combined with the TPD results, we can conclude that there is a more amount of the O₂²⁻ species on the surface of 1.89Pt_{2.20}Mn/TiO₂ at low temperatures, which greatly enhances catalytic activity of the 1.89Pt_{2.20}Mn/TiO₂ for ethylene oxidation.

3.4. Effects of CO₂ and H₂O on catalytic activity

The emitted organic exhaust in the storage and transportation

usually contains CO₂ and H₂O, which are also the products of ethylene oxidation. Hence, it is necessary to examine the effects of CO₂ and H₂O on catalytic activity of the typical sample. Catalytic activities of the 1.89Pt_{2.20}Mn/TiO₂ and 1.91Pt/TiO₂ samples in the presence of 3.0 vol% CO₂ or 50 RH% at $SV = 20,000 \text{ mL}/(\text{g h})$ are shown in Fig. 5. In the case of 3.0 vol% CO₂ addition, ethylene conversions decreased by ca. 5% over 1.89Pt_{2.20}Mn/TiO₂ but by ca. 10% over 1.91Pt/TiO₂; when 3.0 vol% CO₂ was cut off, catalytic activity was restored over the former but not recovered over the latter. That is to say, the introduction of CO₂ to the reaction system did not significantly influence catalytic activity of 1.89Pt_{2.20}Mn/TiO₂, i.e., the doping of Mn to Pt could improve CO₂ resistance of the sample. In the case of water vapor (50 RH%), there was a considerable drop in catalytic activity over each of the two samples. For example, ethylene conversions declined from 90 to ca. 60% over 1.89Pt_{2.20}Mn/TiO₂, and from 90 to ca. 40% over 1.91Pt/TiO₂. After moisture was cut off, ethylene conversions were recovered to their initial levels over 1.89Pt_{2.20}Mn/TiO₂, but only ca. 80% ethylene conversion was retained over 1.91Pt/TiO₂. Therefore, 1.89Pt_{2.20}Mn/TiO₂ possessed much better moisture-resistant performance than 1.91Pt/TiO₂.

3.5. Surface property, adsorption and desorption behavior

Ma et al. [8] reported that the competitive adsorption of H₂O or CO₂ and C₂H₄ at the active sites was the main factor influencing stability of a catalyst. We used the XPS, TGA, pyridine-FTIR, and H₂O- and C₂H₄-TPD techniques to probe the reason why 1.89Pt_{2.20}Mn/TiO₂ was better in stability than 1.91Pt/TiO₂.

XPS was employed to investigate surface element compositions, metal chemical valance, and oxygen species of the samples. Surface element compositions of the 1.89Pt_{2.20}Mn/TiO₂ and 1.91Pt/TiO₂ samples before (1.89Pt_{2.20}Mn/TiO₂-fresh and 1.91Pt/TiO₂-fresh) and after 30 h of ethylene oxidation in the absence (1.89Pt_{2.20}Mn/TiO₂-30 h and 1.91Pt/TiO₂-30 h) or presence (1.89Pt_{2.20}Mn/TiO₂-H₂O and 1.91Pt/TiO₂-H₂O) of water (50 RH%) at $SV = 20,000 \text{ mL}/(\text{g h})$ were measured using the XPS technique, and their C 1s, O 1s, Pt 4f, and Mn 2p_{3/2} XPS spectra and quantitative analysis results are presented in Fig. 6 and S10 and Table 2, respectively. As shown in Fig. S10, the C 1s spectra could be decomposed into three components at binding energy (BE) = 284.8, 284.6, and 288.7 eV, owing to the surface polluted carbon species and surface carbonate species [29,30]. It is observed that the amount of the surface carbonate species increases after 30 h reaction on 1.89Pt_{2.20}Mn/TiO₂ and 1.91Pt/TiO₂. However, the increased amount on 1.89Pt_{2.20}Mn/TiO₂ (from 4.34% to 6.60%) was less than that on 1.91Pt/TiO₂ (from 3.77% to 7.76%). This result indicates that there are more carbonate species deposited on the surface of 1.91Pt/TiO₂ during

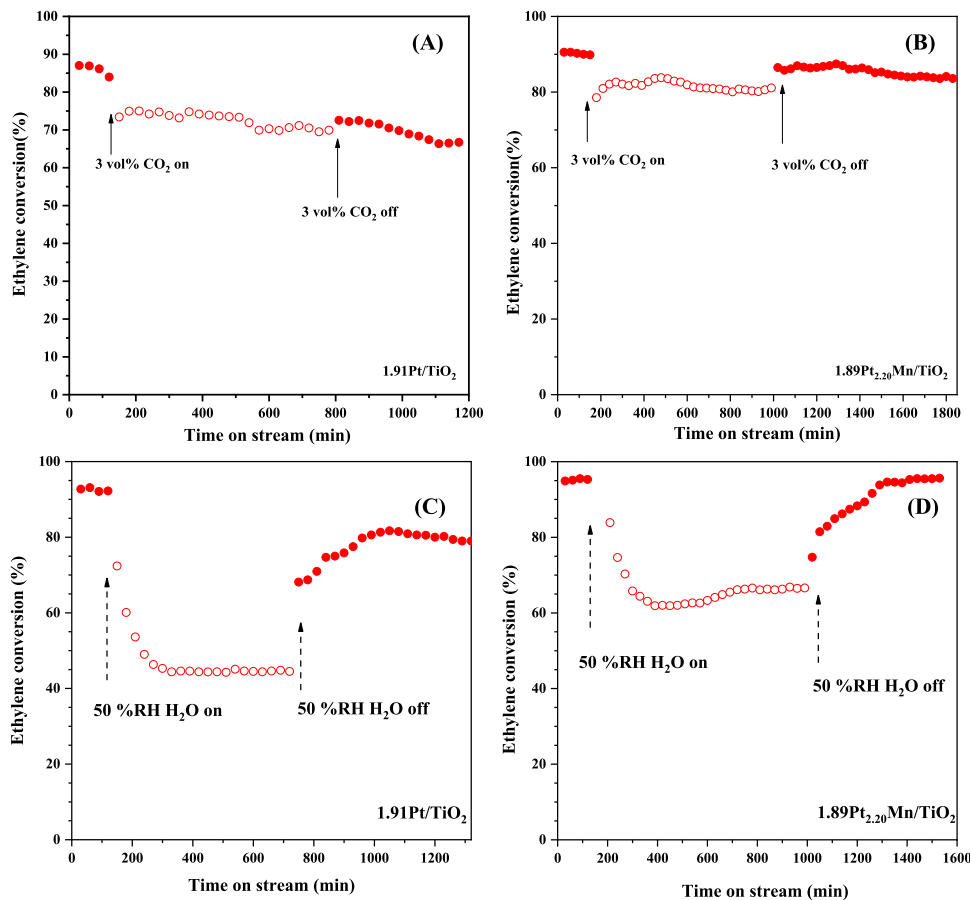


Fig. 5. Effects of (A, B) CO_2 and (C, D) water vapor on catalytic activity of (A, C) $1.91\text{Pt}/\text{TiO}_2$ and (B, D) $1.89\text{Pt}_{2.20}\text{Mn}/\text{TiO}_2$.

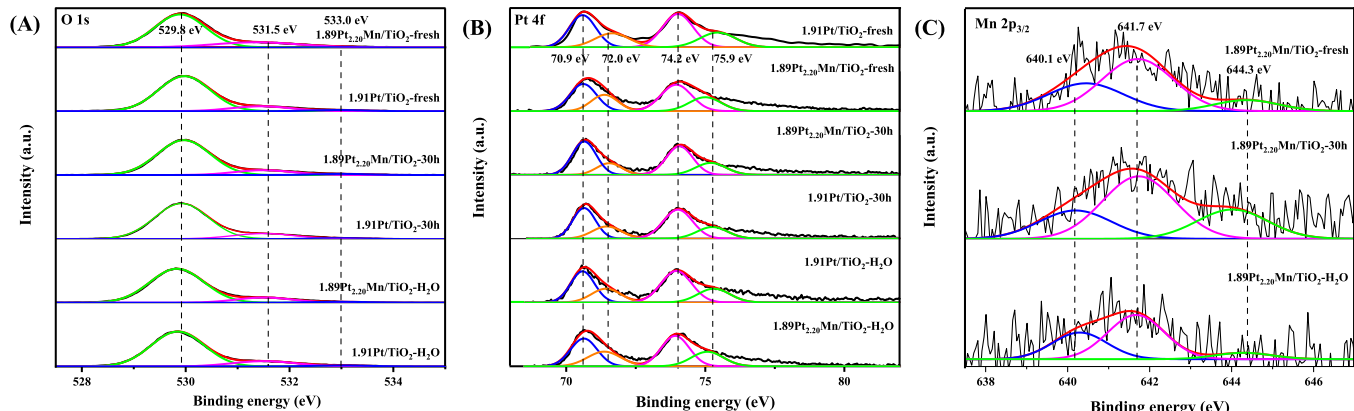


Fig. 6. (A) O 1s, (B) Pt 4f, and (C) Mn 2p_{3/2} XPS spectra of the $1.89\text{Pt}_{2.20}\text{Mn}/\text{TiO}_2$ and $1.91\text{Pt}/\text{TiO}_2$ samples before ($1.89\text{Pt}_{2.20}\text{Mn}/\text{TiO}_2$ -fresh and $1.91\text{Pt}/\text{TiO}_2$ -fresh) and after 30 h of ethylene oxidation in the absence ($1.89\text{Pt}_{2.20}\text{Mn}/\text{TiO}_2$ -30 h and $1.91\text{Pt}/\text{TiO}_2$ -30 h) or presence ($1.89\text{Pt}_{2.20}\text{Mn}/\text{TiO}_2\text{-H}_2\text{O}$ and $1.91\text{Pt}/\text{TiO}_2\text{-H}_2\text{O}$) of 50 RH% water at $\text{SV} = 20,000 \text{ mL}/(\text{g h})$.

the ethylene oxidation process. Shown in Fig. 6A are O 1s spectra of the $1.89\text{Pt}_{2.20}\text{Mn}/\text{TiO}_2$ -fresh, $1.91\text{Pt}/\text{TiO}_2$ -fresh, $1.89\text{Pt}_{2.20}\text{Mn}/\text{TiO}_2$ -30 h, $1.91\text{Pt}/\text{TiO}_2$ -30 h, $1.89\text{Pt}_{2.20}\text{Mn}/\text{TiO}_2\text{-H}_2\text{O}$, and $1.91\text{Pt}/\text{TiO}_2\text{-H}_2\text{O}$ samples, in each of which there was an asymmetrical signal that could be decomposed into three components at BE = 529.8, 531.5, and 533.0 eV, attributable to the surface lattice oxygen (O_{latt}), adsorbed oxygen (O_{ads}), and adsorbed water or carbonate species [31,32], respectively. After 30 h of reaction, the $\text{O}_{\text{ads}}/\text{O}_{\text{latt}}$ molar ratio on $1.89\text{Pt}_{2.20}\text{Mn}/\text{TiO}_2$ decreased from 0.25 to 0.21, whereas that on $1.91\text{Pt}/\text{TiO}_2$ decreased from 0.16 to 0.13; after 10 h of ethylene oxidation in the presence of 50

RH% water, the $\text{O}_{\text{ads}}/\text{O}_{\text{latt}}$ molar ratio on the former further increased from 0.25 to 0.26, and that on the latter also increased from 0.16 to 0.18 (Table 2). The results indicate that the amount of the O_{ads} concentration increases on the two samples, i.e., the introduced water is transformed to the active oxygen species that can be involved in the oxidation of ethylene. In addition, a more amount of O_{ads} was observed on $1.89\text{Pt}_{2.20}\text{Mn}/\text{TiO}_2$ than on $1.91\text{Pt}/\text{TiO}_2$, thus rendering the former to outperform the latter in ethylene oxidation.

As illustrated in Fig. 6B, there were two asymmetrical Pt 4f signals that could be decomposed into four components at BE = 70.9, 72.0,

Table 2
Surface element compositions of the as-obtained samples.

Sample	Pt ²⁺ /Pt ⁰ ^a (mol/mol)	O _{ads} /O _{latt} ^a (mol/mol)	Mn ²⁺ ^a (mol%)	Mn ³⁺ ^a (mol%)	Mn ⁴⁺ ^a (mol%)
1.89Pt _{2.20} Mn/TiO ₂ -fresh	0.65	0.25	26.5	65.1	8.4
1.89Pt _{2.20} Mn/TiO ₂ -30 h	0.97	0.21	23.0	52.6	24.4
1.89Pt _{2.20} Mn/TiO ₂ -H ₂ O	0.66	0.26	29.8	61.7	8.5
1.91Pt/TiO ₂ -fresh	0.70	0.16	—	—	—
1.91Pt/TiO ₂ -30 h	0.97	0.13	—	—	—
1.91Pt/TiO ₂ -H ₂ O	0.70	0.18	—	—	—

^a Determined by the XPS technique

74.2, and 75.9 eV, among which the two components at BE = 70.9 and 74.2 eV were assignable to the surface metallic Pt (Pt⁰) species, while those at BE = 72.0 and 75.9 eV were attributable to the surface oxidized Pt (Pt²⁺) species [33,34]. Based on the results of XPS (Table 2) and XAFS characterization, we can conclude that the Pt on the surface of 1.89Pt_{2.20}Mn/TiO₂ or 1.91Pt/TiO₂ is present in the form of Pt⁰ and Pt²⁺, whereas the Pt in the bulk of the two samples exists in the form of Pt⁰. Similar to the XAFS results, there were more Pt⁰ species in the 1.89Pt_{2.20}Mn/TiO₂ sample, which might be resulted from the transfer of electrons from MnO_x to Pt. After 30 h of ethylene oxidation, the Pt²⁺/Pt⁰ molar ratios on 1.89Pt_{2.20}Mn/TiO₂ and 1.91Pt/TiO₂ increased from 0.65 and 0.70–0.97 and 0.97, respectively, but no significant alterations (0.65–0.66 and 0.70–0.70 on 1.89Pt_{2.20}Mn/TiO₂ and 1.91Pt/TiO₂, respectively) in Pt²⁺/Pt⁰ molar ratio were observed after 10 h of ethylene oxidation in the presence of 50 RH% water. The results reveal that the surface Pt⁰ species concentration decreases after the reaction (the Pt⁰ species were oxidized to the Pt²⁺ species), but the introduction of water did not induce a significant effect on Pt²⁺/Pt⁰ molar ratio. The metallic platinum (Pt⁰) was thought to be the active sites in the oxidation of VOCs [35,36]. As reported by some authors [37,38], the metallic Pt⁰ species in the bimetallic catalysts were also considered as the active sites for the adsorption of oxygen, whereas the transition metal oxide (MO_x) in the bimetallic catalysts were regarded as the active sites for the activation and adsorption of VOCs. In the present work, the electron-rich Pt in 1.89Pt_{2.20}Mn/TiO₂ could activate O₂ to the active electrophilic oxygen species (O₂^{·-}) [22], whereas the MnO_x adjacent to Pt possessed the function of adsorbing and activating ethylene.

The asymmetrical Mn 2p_{3/2} signals could be deconvoluted into three components at BE = 640.1, 641.7, and 644.3 eV (Fig. 6C), among which the first two components at BE = 640.1 and 641.7 eV were ascribable to the surface Mn²⁺ and Mn³⁺ species, respectively, whereas the third one at BE = 644.3 eV was due to the surface Mn⁴⁺ species [39,40]. After quantitative analysis on the Mn 2p_{3/2} spectra of 1.89Pt_{2.20}Mn/TiO₂, we can realize that there is the co-presence of Mn²⁺ (26.5%), Mn³⁺ (65.1%), and Mn⁴⁺ (8.4%) on 1.89Pt_{2.20}Mn/TiO₂-fresh, Mn²⁺ (23.0%), Mn³⁺ (52.6%), and Mn⁴⁺ (24.4%) on 1.89Pt_{2.20}Mn/TiO₂-30 h, and Mn²⁺ (29.8%), Mn³⁺ (61.7%), and Mn⁴⁺ (8.5%) on 1.89Pt_{2.20}Mn/TiO₂-H₂O. Obviously, the surface Mn²⁺ and Mn³⁺ concentrations decreased but the surface Mn⁴⁺ concentration significantly increased after 30 h of ethylene oxidation; after 10 h of ethylene oxidation in the presence of 50 RH% water, however, the surface Mn²⁺ concentration increased, the surface Mn³⁺ concentration decreased slightly, but the surface Mn⁴⁺ concentration was almost unaltered.

Shown in Fig. S11 are TGA profiles of the 1.91Pt/TiO₂ and 1.89Pt_{2.20}Mn/TiO₂ samples before and after 30 h of ethylene oxidation at SV = 20,000 mL/(g h). It is observed that there is no considerable difference in the profile of weight loss versus temperature in the fresh

and used 1.89Pt_{2.20}Mn/TiO₂ samples, suggesting that no significant CO₂ adsorption takes place on the surface of 1.89Pt_{2.20}Mn/TiO₂. The weight loss of the used 1.91Pt/TiO₂-30 h sample was remarkably higher than that of its fresh counterpart at ca. 200 °C, and such a difference in weight loss increased with the rise in temperature. This result demonstrates that there is significant CO₂ adsorption on the surface of the used 1.91Pt/TiO₂ sample.

Fig. 7 shows pyridine-FTIR spectra of pyridine adsorption at different temperatures over the fresh and used (after 30 h of ethylene oxidation at SV = 20,000 mL/(g h)) 1.91Pt/TiO₂ and 1.89Pt_{2.20}Mn/TiO₂ samples. There were several absorption bands in each spectrum. The band at 1643 cm⁻¹ was assignable to the pyridine adsorbed at the Brønsted acid sites, the one at 1444 cm⁻¹ was ascribable to the pyridine adsorbed at the Lewis acid sites, while the one at 1491 cm⁻¹ was assignable to both Brønsted and Lewis acid sites [41]. After quantitatively analyzing the bands, we can obtain amounts of the Brønsted and Lewis acid sites, as listed in Table 3. It is observed that the amounts of the Lewis acid sites in the fresh 1.91Pt/TiO₂ and 1.89Pt_{2.20}Mn/TiO₂ samples were close, but the former sample possessed a slightly more amount of the Brønsted acid sites than the latter sample. After 30 h of ethylene oxidation, the total acid amounts and Brønsted acid amounts in both samples were more than their fresh counterparts, and the amount of the Lewis acid sites in 1.89Pt_{2.20}Mn/TiO₂ decreased but that in 1.91Pt/TiO₂ increased. For example, the total amount of the Brønsted and Lewis acid sites in 1.89Pt_{2.20}Mn/TiO₂ increased from 0.13 to 0.39, and that in 1.91Pt/TiO₂ increased from 0.17 to 0.55 after 30 h of ethylene oxidation. The more significant increase in amount of the Brønsted acid sites in 1.91Pt/TiO₂ might be due to deposition of a more amount of the carbonate species. Such a result was in good agreement with the outcomes of XPS and TGA characterization.

As stated above, CO₂ adsorption was one of the factors influencing stability of the samples. We further probe the effect of water vapor on stability of the samples. Water can interact with the coordination-unsaturated Ti cation through the two pathways: (i) the associated adsorption of proton and –OH; and (ii) bonding of proton with surface oxygen atom as well as bonding of –OH with surface Ti cation. Fig. 8A shows H₂O-TPD profiles of the 1.89Pt_{2.20}Mn/TiO₂ and 1.91Pt/TiO₂ samples, in which each profile could be decomposed into six peaks at 127, 188, 283, 348, 372, and 436 °C. The peaks at 120–150 °C was due to the water species physically adsorbed on the samples, the ones at 150–300 °C were due to the surface water species associatively adsorbed on the samples, and the ones above 300 °C were due to dehydration of hydroxide species [42,43]. According to the literature [44], the interaction of water vapor and surface active oxygen species (O₂^{·-} or O[·] + H₂O → 2 –OH) generated surface hydroxyl groups that could be involved in the oxidation of hydrocarbons [44]. The associatively adsorbed water species might be the active sites for the oxidation of ethylene since they could provide the active protons [7,45]. Table S2 summarizes the contents of the water species adsorbed on the samples. The contents of the physically adsorbed water, associatively adsorbed water, and water dehydrated from the hydroxide species on the 1.89Pt_{2.20}Mn/TiO₂ sample were 8.49%, 60.25%, and 31.26%, whereas those on the 1.91Pt/TiO₂ sample were 9.06%, 57.00%, and 33.94%, respectively. The associatively adsorbed water content on 1.91Pt/TiO₂ was lower than that on 1.89Pt_{2.20}Mn/TiO₂. Based on the above analysis, we can realize that the associatively adsorbed water was likely to be the active oxygen species, which were formed in the oxygen vacancies in the samples [46,47]. Therefore, the hydroxyl groups formed due to the associatively adsorbed water in the oxygen vacancies of the samples might involve in the oxidation of ethylene.

We used the ethylene-TPD (C₂H₄-TPD) technique to investigate the adsorbed ethylene species and competitive adsorption of ethylene and water on the fresh and H₂O-adsorbed 1.89Pt_{2.20}Mn/TiO₂ and 1.91Pt/TiO₂ samples, and their profiles are shown in Fig. 8B and C. Each profile could be decomposed into five peaks at 75, 107, 215, 320, and 384 °C, among which the peaks at 75 and 107 °C were due to the physically

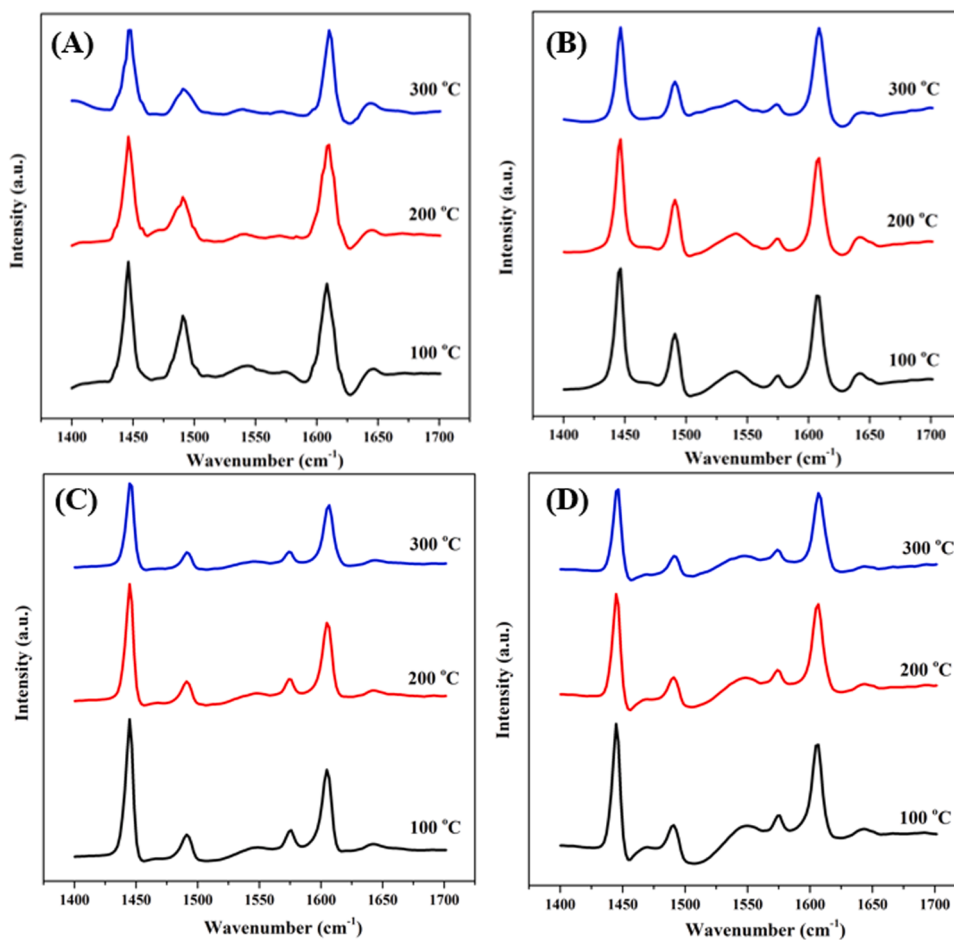


Fig. 7. Pyridine-FTIR spectra of (A) 1.91Pt/TiO₂, (B) 1.91Pt/TiO₂-used, (C) 1.89Pt_{2.20}Mn/TiO₂, and (D) 1.89Pt_{2.20}Mn/TiO₂-used after pyridine adsorption at different temperatures.

Table 3
Acid amounts of the samples measured by the pyridine-FTIR technique.

Sample	C (L) ^a ($\mu\text{mol/g}$)	C (B) ^b ($\mu\text{mol/g}$)	Total acid amount ($\mu\text{mol/g}$)	C (B)/C (L)
1.89Pt _{2.20} Mn/TiO ₂	119.4	16.3	135.7	0.13
1.91Pt/TiO ₂	118.5	20.2	138.7	0.17
1.89Pt _{2.20} Mn/ TiO ₂ -used	108.9	42.9	151.7	0.39
1.91Pt/TiO ₂ -used	124.5	69.0	193.5	0.55

^a C(L) was the amount of the Lewis acid sites obtained after the desorption of pyridine at 100 °C.

^b C(B) was the amount of the Bronsted acid sites obtained after the desorption of pyridine at 100 °C.

adsorbed ethylene (Type a) species, the one at 215 °C was due to the weakly chemically adsorbed ethylene (Type b) species, and the ones at 320 and 384 °C were due to the strongly chemically adsorbed ethylene (Type c) species [48,49]. Ethylene was significantly physically and chemically adsorbed on the 1.89Pt_{2.20}Mn/TiO₂ sample (Fig. 8B), but only remarkably strongly chemical adsorption took place on the 1.91Pt/TiO₂ sample (Fig. 8C). By comparing Fig. 8B and C, we can realize that the adsorption capacity of ethylene on 1.89Pt_{2.20}Mn/TiO₂ is much higher than that on 1.91Pt/TiO₂, even more than ten times. Besides, the latter possessed a significantly decreased ethylene adsorption amount than the former at low temperature (Table S3), in which only one desorption peak at 384 °C was recorded in the 1.91Pt/TiO₂ sample. The larger adsorption capacity and more ethylene desorption peaks indicate that the introduction of Mn provides more active sites for

ethylene adsorption and activation, which would reduce the inhibitory effect of adsorbed water on ethylene adsorption. The better performance of the H₂O-adsorbed 1.89Pt_{2.20}Mn/TiO₂ sample than the 1.91Pt/TiO₂ sample was due to the more amount of ethylene adsorption sites in the former than that in the latter.

To explore the role of water molecules in the oxidation of ethylene over the samples, H₂¹⁸O isotope tracing experiments were conducted. Fig. 9 and S12 show the product distributions of ethylene oxidation in the absence or presence of H₂¹⁸O over 1.89Pt_{2.20}Mn/TiO₂ and 1.91Pt/TiO₂, respectively. Apparently, water was directly involved in the oxidation of ethylene. Ethylene oxidation generated the products of C¹⁶O₂, C¹⁶O¹⁸O, and C¹⁸O₂, with the C¹⁶O¹⁸O being the main product, which substantiated the involvement of water in the oxidation of ethylene. The amounts of the C¹⁶O¹⁸O and C¹⁸O₂ products over 1.89Pt_{2.20}Mn/TiO₂ were higher than those over 1.91Pt/TiO₂. This result indicates that more water molecules are involved in ethylene oxidation. The ¹⁶O¹⁸O and ¹⁸O₂ species were also detected in ethylene oxidation over the two samples in the presence of H₂¹⁸O, which confirms that the oxygen exchange takes place between the oxygen in molecular O₂ or the surface lattice oxygen species and the oxygen in H₂¹⁸O. Wang et al. [50] reported that H₂O could enhance the oxidation of CO over the Pt₁/CeO₂ catalyst, in which the CO adsorbed on the Pt surface was associatively combined with the –OH on the CeO₂ support to form –COOH that was then reacted with the lattice oxygen species to produce CO₂ and H₂O. The whole process could proceed more readily than the reaction of CO with the lattice oxygen species. According to the results of H₂O-TPD and C₂H₄-TPD characterization, we deduce that H₂O is adsorbed on the sample surface to form –OH that reacts with the adsorbed ethylene on

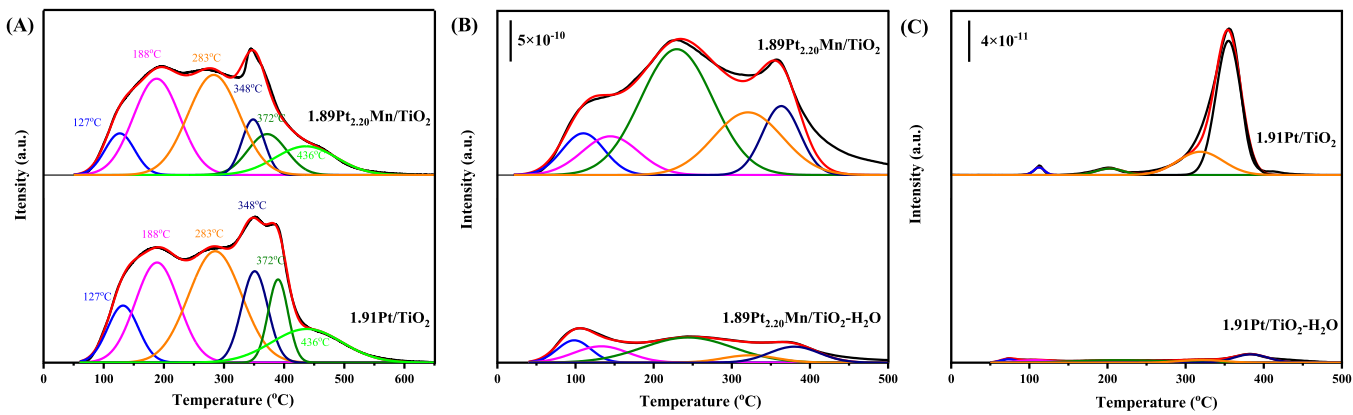


Fig. 8. (A) H_2O - and (B, C) C_2H_4 -TPD profiles of the fresh and H_2O -adsorbed $1.89\text{Pt}_{2.20}\text{Mn}/\text{TiO}_2$ and $1.91\text{Pt}/\text{TiO}_2$ samples.

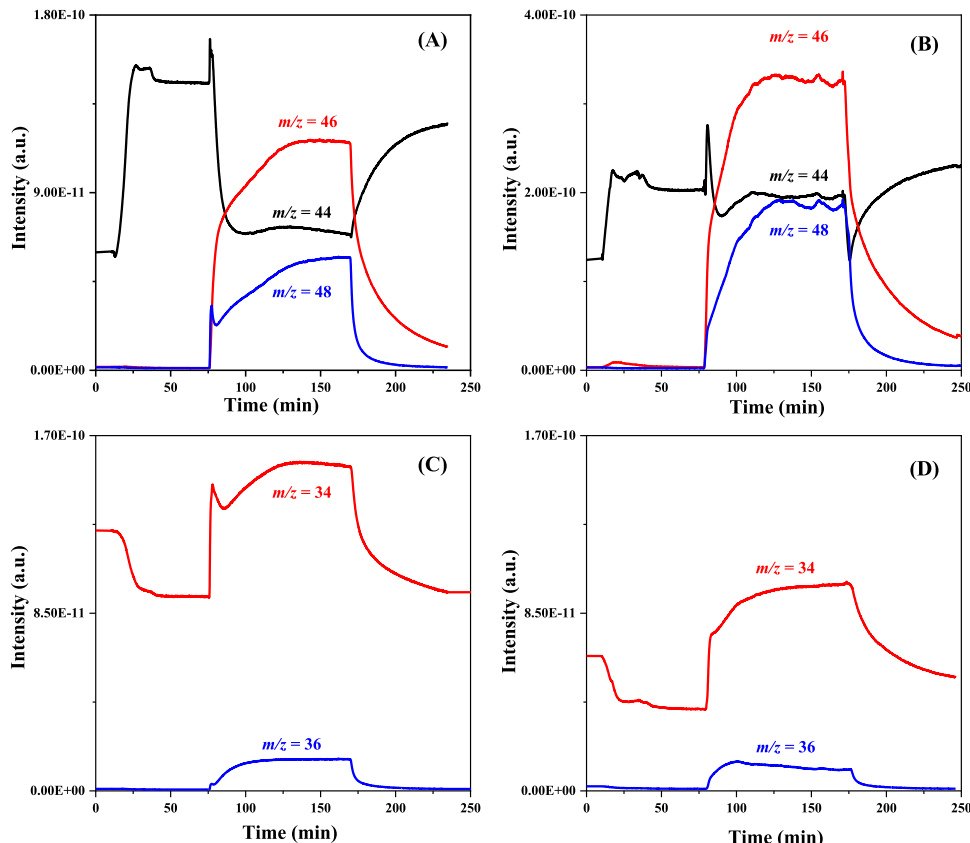


Fig. 9. Time-dependent MS spectra of the pulses of C^{16}O_2 , $\text{C}^{16}\text{O}^{18}\text{O}$, and C^{18}O_2 in the direct C_2H_4 oxidation over (A, C) $1.91\text{Pt}/\text{TiO}_2$ and (B, D) $1.89\text{Pt}_{2.20}\text{Mn}/\text{TiO}_2$.

the sample to generate carbon dioxide and water. The $1.89\text{Pt}_{2.20}\text{Mn}/\text{TiO}_2$ sample possessed a large ethylene adsorption capacity and a more amount of the active sites, furthermore there was a more amount of the adsorbed water species exchangeable with O_2 and reactive toward ethylene, which rendered the generated $\text{C}^{16}\text{O}^{18}\text{O}$ and $\text{C}^{18}\text{O}^{18}\text{O}$ amounts on $1.89\text{Pt}_{2.20}\text{Mn}/\text{TiO}_2$ to be more than those on $1.91\text{Pt}/\text{TiO}_2$, thus making the former show better catalytic performance and stability than the latter in ethylene oxidation. Combined with the results of Raman, H_2O - and C_2H_4 -TPD characterization, we can realize that compared with $1.91\text{Pt}/\text{TiO}_2$, $1.89\text{Pt}_{2.20}\text{Mn}/\text{TiO}_2$ possessed more amounts of the active sites for ethylene adsorption and oxygen species (such as, O_2^2) and involving in ethylene oxidation, which gave rise to more amounts of $\text{C}^{16}\text{O}^{18}\text{O}$ and C^{18}O_2 over $1.89\text{Pt}_{2.20}\text{Mn}/\text{TiO}_2$ than those over $1.91\text{Pt}/\text{TiO}_2$, hence the former sample was better in catalytic

activity and stability than the latter sample.

3.6. Catalytic oxidation mechanism

To study the catalytic ethylene oxidation mechanisms, we used the in situ DRIFTS technique to investigate ethylene oxidation over the $1.89\text{Pt}_{2.20}\text{Mn}/\text{TiO}_2$ and $1.91\text{Pt}/\text{TiO}_2$ samples at different time and temperatures, and their in situ DRIFTS spectra are shown in Fig. 10. The absorption band at 2042 or 2090 cm^{-1} was assigned to the CO species [51], and the ones at 1440 and 1574 cm^{-1} were ascribed to the physical adsorption of formic acid and adsorption of formate species [51], respectively. The absorption bands at 1640 and 3219 or 3403 cm^{-1} were assigned to the H_2O and OH species, and the ones at 2986 and 3087 cm^{-1} were ascribed to the physical and chemical adsorption of

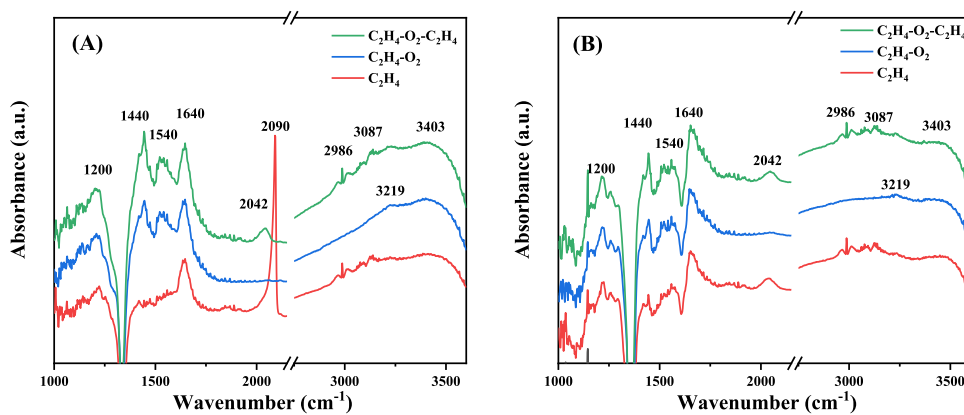


Fig. 10. In situ DRIFTS spectra of ethylene oxidation at different atmospheres over (A) 1.89Pt_{2.20}Mn/TiO₂ and (B) 1.91Pt/TiO₂.

ethylene or formic acid [51,52], respectively. With the introduction of ethylene and oxygen, vibration bands of formic acid, CO, CO₂, and etc. appeared on the surface of the sample. It can be inferred that ethylene oxidation takes place according to the pathways of ethylene → formaldehyde → formic acid → CO₂ and H₂O, in good consistency with the results reported in the literature [51–53]. The band assigned to the CO species on 1.91Pt/TiO₂ was slightly shifted to a higher wavenumber (2090 cm⁻¹) on 1.89Pt_{2.20}Mn/TiO₂. A higher wavenumber means a higher CO coverage [51]. Meanwhile, intensity of the CO vibration band on 1.89Pt_{2.20}Mn/TiO₂ was much stronger than that on 1.91Pt/TiO₂. Hence, ethylene on the surface of 1.89Pt_{2.20}Mn/TiO₂ was more easily oxidized to generate CO. Combining the results of Raman and C₂H₄-TPD (Fig. 4) characterization, it can be inferred that the peroxide species (O₂²⁻) on the surface of 1.89Pt_{2.20}Mn/TiO₂ promotes the oxidation of ethylene. In addition, after the initial introduction of ethylene, there was no vibration band of the formic acid species on the surface of 1.89Pt_{2.20}Mn/TiO₂, indicating that the peroxide species can promote the oxidation of ethylene to CO. Subsequently, CO could quickly be oxidized to CO₂ after introducing oxygen.

In situ DRIFTS spectra of the samples in the reaction atmosphere are shown in Fig. S13. With the extension of adsorption time, the amount of ethylene adsorbed on the 1.89Pt_{2.20}Mn/TiO₂ or 1.91Pt/TiO₂ sample increased. It can be seen from Fig. S13(A, B) that intensity of ethylene adsorption bands on 1.89Pt_{2.20}Mn/TiO₂ is higher than that on 1.91Pt/TiO₂, demonstrating that the former possesses a more amount of the active sites for the adsorption of ethylene than the later. This result was in good agreement with that of C₂H₄-TPD characterization.

4. Conclusions

Pt_xMn_y nanocrystals were prepared by oil-phase reduction method. Among all of the samples, 1.89Pt_{2.20}Mn/TiO₂ performed the best for ethylene oxidation: $T_{50\%} = 34$ °C and $T_{90\%} = 43$ °C at SV = 20,000 mL/(g h), specific reaction rate at 35 °C = 33.0 $\mu\text{mol}/(\text{g}_{\text{Pt}} \text{s})$, and turnover frequency at 35 °C = $6.5 \times 10^{-3} \text{ s}^{-1}$. In addition, 1.89Pt_{2.20}Mn/TiO₂ exhibited better water resistance and stability than 1.91Pt/TiO₂. Such an improvement in water resistance and stability induced by ultrasmall MnO_x cluster/Pt hetero-junction was investigated using the XPS, H₂O-TPD, C₂H₄-TPD, in situ DRIFTS, and H₂¹⁸O isotopic tracing techniques. It was found that the fabricating of MnO_x layers on Pt particles inhibited the adsorption of CO₂, and enhanced the surface active oxygen species (O₂²⁻). And the plentiful MnO_x/Pt interfaces provide more active sites for the adsorption and activation of ethylene, reducing the inhibitory effect of adsorbed water on ethylene adsorption.

CRediT authorship contribution statement

Zhiqian Hou and Meiqi Chen: Writing – review & editing,

Investigation. Yuxi Liu: Investigation, Methodology, Supervision, Project administration. Jiguang Deng: Investigation. Lin Jing: Investigation. Ruyi Gao: Investigation, Data curation. Wenbo Pei: Investigation, Data curation. Zeya Li: Investigation, Data curation. Hongxing Dai: Writing – review & editing, Methodology, Supervision, Project administration.

Declaration of Competing Interest

The authors declare that they have no known competing financial interests or personal relationships that could have appeared to influence the work reported in this paper.

Data availability

No data was used for the research described in the article.

Acknowledgements

This work was financially supported by National Natural Science Committee of China-Liaoning Provincial People's Government Joint Fund (U1908204), the State's Key Project of Research and Development Plan (2022YFB3506200 and 2022YFB3504101), National Natural Science Foundation of China (21976009), Beijing Natural Science Foundation (J210006), and Research and Development Program of Beijing Municipal Education Commission (KZ202210005011).

Appendix A. Supporting information

Supplementary data associated with this article can be found in the online version at doi:10.1016/j.apcatb.2023.123115.

References

- [1] H.G. Ahn, B.M. Choi, D.J. Lee, Complete oxidation of ethylene over supported gold nanoparticle catalysts, *J. Nanosci. Nanotechnol.* 6 (2006) 3599–3603.
- [2] W.C. Li, Z.X. Zhang, J.T. Wang, W.M. Qiao, D.H. Long, L.C. Ling, Low temperature catalytic combustion of ethylene over cobalt oxide supported mesoporous carbon spheres, *Chem. Eng. J.* 293 (2016) 243–251.
- [3] R.J. Isaifan, N. Spyridon, B. Elena, Particle size effect on catalytic activity of carbon-supported Pt nanoparticles for complete ethylene oxidation, *Appl. Catal. A* 464 (2013) 87–94.
- [4] J.J. Li, C.Y. Ma, X.Y. Xu, J.J. Yu, Z.P. Hao, S.Z. Qiao, Efficient elimination of trace ethylene over nano-gold catalyst under ambient conditions, *Environ. Sci. Technol.* 42 (2008) 8947–8951.
- [5] C.Y. Ma, Z. Mu, J.J. Li, Y.G. Jin, J. Cheng, G.Q. Lu, Z.P. Hao, S.Z. Qiao, Mesoporous Co₃O₄ and Au/Co₃O₄ catalysts for low-temperature oxidation of trace ethylene, *J. Am. Chem. Soc.* 132 (2010) 2608–2613.
- [6] W.J. Xue, Y.F. Wang, P. Li, Z.T. Liu, Z.P. Hao, C.Y. Ma, Morphology effects of Co₃O₄ on the catalytic activity of Au/Co₃O₄ catalysts for complete oxidation of trace ethylene, *Catal. Commun.* 12 (2011) 1265–1268.

[7] H. Yang, C.Y. Ma, X. Zhang, Understanding the active sites of Ag/zeolites and deactivation mechanism of ethylene catalytic oxidation at room temperature, *ACS Catal.* 8 (2018) 1248–1258.

[8] H. Yang, C.Y. Ma, X. Zhang, Synthesis, characterization and evaluations of the Ag/ZSM-5 for ethylene oxidation at room temperature: Investigating the effect of water and deactivation, *Chem. Eng. J.* 347 (2018) 808–818.

[9] H. Yang, C.Y. Ma, G. Wang, Fluorine-enhanced Pt/ZSM-5 catalysts for low-temperature oxidation of ethylene, *Catal. Sci. Technol.* 8 (2018) 1988–1996.

[10] Y. Kang, J.B. Pyo, X.C. Ye, T. Gordon, Synthesis, shape control and methanol electro-oxidation properties of PtZn alloy and Pt₃Zn intermetallic nanocrystals, *ACS Nano* 6 (2012) 5642–5647.

[11] K. Adamskaa, J. Okal, W. Tylus, Stable bimetallic Ru-Mo/Al₂O₃catalysts for the light alkane combustion: Effect of the Mo addition, *Appl. Catal. B* 246 (2019) 180–194.

[12] S. Hinokuma, N. Yamashita, Y. Katsuhara, H. Kogamia, M. Machida, CO oxidation activity of thermally stable Fe–Cu/CeO₂ catalysts prepared by dual-mode arc-plasma process, *Catal. Sci. Technol.* 5 (2015) 3945–3952.

[13] V. Mazumder, M.F. Chi, S.H. Sun, A facile synthesis of MPd (M = Co, Cu) nanoparticles and their catalysis for formic acid oxidation, *Nano Lett.* 12 (2012) 1102–1106.

[14] T. Ishihara, K. Eguchi, H. Arai, Hydrogenation of carbon monoxide over SiO₂-supported Fe-Co, Co-Ni and Ni-Fe bimetallic catalysts, *Appl. Catal. A* 30 (1987) 225–238.

[15] S. Furukawa, K. Ehara, T. Komatsu, Unique reaction mechanism of preferential oxidation of CO over intermetallic Pt₃Co catalysts: Surface-OH-mediated formation of a bicarbonate intermediate, *Catal. Sci. Technol.* 6 (2016) 1642–1650.

[16] H.Y. Zhu, Z.L. Wu, D. Su, G.M. Veith, H.F. Lu, Constructing hierarchical interfaces: TiO₂ supported PtFe–FeO_x nanowires for room temperature CO oxidation, *J. Am. Chem. Soc.* 137 (2015) 10156–10159.

[17] S. Rojuechai, S. Chavadej, J.W. Schwank, V. Meeyoo, Catalytic activity of ethylene oxidation over Au, Ag and Au–Ag catalysts: Support effect, *Catal. Commun.* 8 (2007) 57–64.

[18] J. Yang, Y.X. Liu, J.G. Deng, S.H. Xie, Z.H. Hou, X.T. Zhao, K.F. Zhang, Z. Han, H. X. Dai, Pt_xCo/meso-MnO_y: highly efficient catalysts for low-temperature methanol combustion, *Catal. Today* 332 (2019) 168–176.

[19] S.H. Xie, J.G. Deng, S.M. Zang, H.G. Yang, G.S. Guo, H. Arandiyani, H.X. Dai, Au–Pd/3DOM Co₃O₄: highly active and stable nanocatalysts for toluene oxidation, *J. Catal.* 322 (2015) 38–48.

[20] Z.Q. Hou, Y.X. Liu, J.G. Deng, Y. Lu, S.H. Xie, X.Z. Fang, H.X. Dai, Highly active and stable Pd–GaO_x/Al₂O₃ catalysts derived from intermetallic Pd₂Ge₃ nanocrystals for methane combustion, *ChemCatChem* 24 (2018) 5637–5648.

[21] Y.J. Liang, Y.X. Liu, J. Deng, K.F. Zhang, Z.Q. Hou, X.T. Zhao, X. Zhang, K. Y. Zhang, R.J. Wei, H.X. Dai, Coupled palladium–tungsten bimetallic nanosheets/TiO₂ hybrids with enhanced catalytic activity and stability for the oxidative removal of benzene, *Environ. Sci. Technol.* 53 (2019) 5926–5935.

[22] K.Y. Zhang, L.Y. Dai, Y.X. Liu, J.G. Deng, L. Jing, K.F. Zhang, Z.Q. Hou, X. Zhang, J. Wang, Y. Feng, Y.X. Zhang, H.X. Dai, Insights into the active sites of chlorine-resistant Pt-based bimetallic catalysts for benzene oxidation, *Appl. Catal. B* 279 (2020), 119372.

[23] T.T. Chao, X. Luo, W.X. Chen, B. Jiang, J.J. Ge, Y. Lin, G. Wu, X.Q. Wang, Y.M. Hu, Z.B. Zhuang, Y. Wu, X. Hong, Y.D. Li, Atomically dispersed copper–platinum dual sites alloyed with palladium nanorings catalyze the hydrogen evolution reaction, *Angew. Chem. Int. Ed.* 56 (2017) 16047–16051.

[24] J.T. Miller, A.J. Kropf, Y. Zhai, J.R. Regalbuto, L. Delannoy, C. Louis, E. Bus, J. A. van Bokhoven, The effect of gold particle size on Au–Au bond length and reactivity toward oxygen in supported catalysts, *J. Catal.* 240 (2006) 222–234.

[25] E.A. Elimian, M. Zhang, J. Chen, H.P. Jia, Y. Sun, J. He, Construction of Pt-mTiO₂/USY multifunctional catalyst enriched with oxygen vacancies for the enhanced light-driven photothermocatalytic degradation of toluene, *Appl. Catal. B* 307 (2022), 121203.

[26] A.G. Ilie, M. Scarisoareanu, I. Morjan, E. Dutu, M. Badiceanu, I. Mihailescu, Principal component analysis of Raman spectra for TiO₂ nanoparticle characterization, *Appl. Surf. Sci.* 417 (2017) 93–103.

[27] C.T. Au, H. He, S.Y. Lai, C.F. Ng, The oxidative coupling of methane over BaCO₃/LaOBr catalysts of high ethylene yield, *J. Catal.* 163 (1996) 399–408.

[28] T.C. Pu, A. Setiawan, B.M. Lis, M.H. Zhu, M.E. Ford, S. Rangarajan, I.E. Wachs, Nature and reactivity of oxygen species on/in silver catalysts during ethylene oxidation, *ACS Catal.* 12 (2022) 4375–4381.

[29] G.J. Zou, L. Chen, X.L. Wang, A novel grind process to synthesize nano-micron structured LaMnO₃ for catalytic combustion of methane, *Catal. Lett.* 127 (2009) 444–447.

[30] X.F. Qian, D.T. Yue, Z.Y. Tian, M. Reng, Y. Zhu, M. Kan, T.Y. Zhang, Y.X. Zhao, Carbon quantum dots decorated Bi₂WO₆ nanocomposite with enhanced photocatalytic oxidation activity for VOCs, *Appl. Catal. B* 193 (2016) 16–21.

[31] Y.X. Chen, Z.W. Huang, M.J. Zhou, Z. Ma, J.M. Chen, X.F. Tang, Single silver adatoms on nanostructured manganese oxide surface: boosting oxygen activation for benzene abatement, *Environ. Sci. Technol.* 51 (2017) 2304–2311.

[32] X.Q. Yang, X.L. Yu, M.Y. Lin, M.F. Ge, Y. Zhao, F.Y. Wang, Interface effect of mixed phase Pt/ZrO₂ catalyst for HCHO oxidation at ambient temperature, *J. Master. Chem. A* 5 (2017) 13799–13806.

[33] Z.B. Wu, Z.Y. Sheng, Y. Liu, H.Q. Wang, J.S. Mo, Deactivation mechanism of PtO_x/TiO₂ photocatalyst towards the oxidation of NO in gas phase, *J. Hazard. Mater.* 185 (2011) 1053–1058.

[34] H.F. Xiong, S. Lin, J. Goetze, P. Pletcher, H. Guo, L. Kovarik, K. Artyushkova, B. M. Weckhuysen, A.K. Datye, Thermally stable and regenerable platinum–tin clusters for propane dehydrogenation prepared by atom trapping on ceria, *Angew. Chem. Int. Ed.* 56 (2017) 1–7.

[35] A.L. Lu, H.L. Sun, N.W. Zhang, L.M. Che, S.Y. Shan, J. Luo, J.B. Zheng, L.F. Yang, D. L. Peng, C.J. Zhong, B.H. Chen, Surface partial-charge-tuned enhancement of catalytic activity of platinum nanocatalysts for toluene oxidation, *ACS Catal.* 9 (2019) 7431–7442.

[36] Y.R. Liu, X. Li, W.M. Liao, A.P. Jia, Y.J. Wang, M.F. Luo, J.Q. Lu, Highly active Pt/BN catalysts for propane combustion: the roles of support and reactant-induced evolution of active sites, *ACS Catal.* 9 (2019) 1472–1481.

[37] S.H. Hakim, C. Sener, A.C. Alba-Rubio, T.M. Gostanian, B.J. O'Neill, F.H. Ribeiro, J.T. Miller, J.A. Dumesic, Synthesis of supported bimetallic nanoparticles with controlled size and composition distributions for active site elucidation, *J. Catal.* 328 (2015) 75–90.

[38] S.H. Xie, Y.X. Liu, J.G. Deng, X.T. Zhao, J. Yang, K.F. Zhang, Z. Han, H.X. Dai, Three-dimensionally ordered macroporous CeO₂-supported Pd@Co nanoparticles: Highly active catalysts for methane oxidation, *J. Catal.* 342 (2016) 17–26.

[39] L.L. Zhao, Z.P. Zhang, Y.S. Liu, X.S. Leng, T.R. Zhang, F.L. Yuan, X.Y. Niu, Y.J. Zhu, Synthesis of CeMnO_x hollow microsphere with hierarchical structure and its excellent catalytic performance for toluene combustion, *Appl. Catal. B* 245 (2019) 502–512.

[40] M. Piumetti, D. Fino, N. Russo, Mesoporous manganese oxides prepared by solution combustion synthesis as catalysts for the total oxidation of VOCs, *Appl. Catal. B* 163 (2015) 277–287.

[41] M.L. Zhu, S. Li, Z.X. Li, X.M. Lu, S.J. Zhang, Investigation of solid catalysts for glycolysis of polyethylene terephthalate, *Chem. Eng. J.* 185–186 (2012) 168–177.

[42] A. Setiawan, E.M. Kennedy, B.Z. Dlugogorski, A.A. Adesina, M. Stockenhuber, The stability of Co₃O₄, Fe₂O₃, Au/Co₃O₄ and Au/Fe₂O₃ catalysts in the catalytic combustion of lean methane mixtures in the presence of water, *Catal. Today* 258 (2015) 276–283.

[43] Y. Wang, F. Wang, Q. Song, Q. Xin, S. Xu, J. Xu, Heterogeneous ceria catalyst with water-tolerant Lewis acidic sites for one-pot synthesis of 1,3-diols via Prins condensation and hydrolysis reactions, *J. Am. Chem. Soc.* 135 (2013) 1506–1515.

[44] J. Wang, P. Zhang, J. Li, C. Jiang, R. Yunus, J. Kim, Room-temperature oxidation of formaldehyde by layered manganese oxide: effect of water, *Environ. Sci. Technol.* 49 (2015) 12372–12379.

[45] C.Y. Ma, C.G. Yang, B. Wang, C. Chen, F.B. Wang, X.L. Yao, M.Y. Song, Effects of H₂O on HCHO and CO oxidation at room-temperature catalyzed by MCo₂O₄ (M = Mn, Ce and Cu) materials, *Appl. Catal. B* 254 (2019) 76–85.

[46] B. Qiu, M. Zhang, L. Wu, J. Wang, Y. Xia, D. Qian, H. Liu, S. Hy, Y. Chen, K. An, Y. Zhu, Z. Liu, Y.S. Meng, Gas-solid interfacial modification of oxygen activity in layered oxide cathodes for lithium-ion batteries, *Nat. Commun.* 7 (2016) 12108.

[47] D.N. Pei, L. Gong, A.Y. Zhang, X. Zhang, J.J. Chen, Y. Mu, H.Q. Yu, Defective titanium dioxide single crystals exposed by high-energy {001} facets for efficient oxygen reduction, *Nat. Commun.* 6 (2015) 8696.

[48] V. Bolis, J. Vedrin, Adsorption and activation of ethene by zeolite-H-ZSM-5, *J. Chem. Soc. Faraday I* 76 (1980) 1606–1616.

[49] J.X. Zhou, Y.C. Zhang, X.W. Guo, A.F. Zhang, X.M. Fei, Removal of C₂H₄ from a CO₂ stream by using AgNO₃-modified Y-zeolites, *Ind. Eng. Chem. Res.* 45 (2006) 6236–6242.

[50] C.L. Wang, X.K. Gu, H. Yan, Y. Lin, J.J. Li, D.D. Liu, W.X. Li, J.L. Lu, Water-mediated Mars-van Krevelen mechanism for CO oxidation on ceria supported single-atom Pt₁ catalyst, *ACS Catal.* 7 (2017) 887–891.

[51] C.X. Jiang, K.J. Hara, A. Fukuoka, Low-temperature oxidation of ethylene over platinum nanoparticles supported on mesoporous silica, *Angew. Chem. Int. Ed.* 52 (2013) 6265–6268.

[52] R. Miyazaki, N. Nakatani, S.V. Levchenko, T. Yokoya, K. Nakajima, K. Hara, A. Fukuoka, J.Y. Hasegawa, DFT mechanistic study on the complete oxidation of ethylene by the silica-supported Pt catalyst: C=C activation via the ethylene dioxide intermediate, *J. Phys. Chem. C* 123 (2019) 12706–12715.